Suzuki *et al. Earth, Planets and Space* (2016) 68:198
DOI 10.1186/s40623-016-0576-0

Earth, Planets and Space

FRONTIER LETTER

Open Access

Waveform inversion for 3-D S-velocity structure of D″ beneath the Northern Pacific: possible evidence for a remnant slab and a passive plume

Yuki Suzuki[1], Kenji Kawai[1*], Robert J. Geller[1], Anselme F. E. Borgeaud[1] and Kensuke Konishi[2]

Abstract

We conduct waveform inversion to infer the three-dimensional (3-D) S-velocity structure in the lowermost 400 km of the mantle (the D″ region) beneath the Northern Pacific region. Our dataset consists of about 20,000 transverse component broadband body-wave seismograms observed at North American stations for 131 intermediate and deep earthquakes which occurred beneath the western Pacific subduction region. We use S, ScS, and other phases that arrive between them. Resolution tests indicate that our methods and dataset can resolve the velocity structure in the target region with a horizontal scale of about 150 km and a vertical scale of about 50 km. The 3-D S-velocity model obtained in this study shows three prominent features: (1) prominent sheet-like lateral high-velocity anomalies up to ~3% faster than the Preliminary Reference Earth Model (PREM) with a thickness of ~200 km, whose lower boundary is ~150 km above the core–mantle boundary (CMB). (2) A prominent low-velocity anomaly block located to the west of the Kamchatka peninsula, which is ~2.5% slower than PREM, immediately above the CMB beneath the high-velocity anomalies. (3) A relatively thin (~300 km) low-velocity structure continuous from the low-velocity anomaly "(2)" to at least 400 km above the CMB. We also detect a continuous low-velocity anomaly from the east of the Kamchatka peninsula at an altitude of 50 km above the CMB to the far east of the Kuril islands at an altitude of 400 km above the CMB. We interpret these features respectively as: (1) remnants of slab material where the bridgmanite to Mg-post-perovskite phase transition may have occurred within the slab, (2, 3) large amounts of hot and less dense materials beneath the cold Kula or Pacific slab remnants just above the CMB which ascend and form a passive plume upwelling at the edge of the slab remnants.

Keywords: D″, S-velocity structure, Tomography, Waveform inversion, Northern Pacific

Background

The D″ region is the lowermost several 100 km of the mantle immediately above the core–mantle boundary (CMB), and its base is in contact with the liquid iron alloy outer core. Since the D″ region is the thermal boundary layer (TBL) at the base of the Earth's mantle, and the solidus of its constituent materials is thought to be close to the mantle geotherm, vertical and lateral variations of temperature and chemical composition associated with the Earth's thermal evolution are expected (e.g., Wysession et al. 1998; Garnero and McNamara 2008; Kawai and Tsuchiya 2009). Previous studies have analyzed observed seismic waveforms and revealed lateral and vertical heterogeneity within D″ beneath Central America (e.g., Hutko et al. 2006; van der Hilst et al. 2007; Kawai et al. 2014), suggesting complex interaction between the paleosubducted slab and the TBL beneath the subduction zone.

The D″ region, especially beneath subduction zones, provides clues for understanding the dynamics of the Earth's mantle, because thermally and chemically distinct slab materials can perturb the temperature and mantle

*Correspondence: kenji@eps.s.u-tokyo.ac.jp
[1] Department of Earth and Planetary Science, School of Science, University of Tokyo, Hongo 7-3-1, Bunkyo-ku, Tokyo 113-0033, Japan
Full list of author information is available at the end of the article

flow. Hence, it is important to study the D″ region beneath subduction zones to investigate how slabs have subducted to the lowermost mantle. Lay and Helmberger (1983) and Young and Lay (1990) studied seismic structure in D″ in particular regions beneath the circum-Pacific, especially beneath the Northern Pacific, and proposed 1-D S-velocity structure models, SLHO and SYLO, respectively, which have a positive velocity jump about 240 km above the CMB and a negative velocity gradient beneath the discontinuity. He et al. (2014) suggested an 850-km-thick low-velocity anomaly surrounded by a 210-km-thick high-velocity anomaly in D″ beneath Kamchatka on the basis of forward modeling of seismic waveforms. Sun et al. (2016) studied the lowermost mantle beneath Alaska using waveforms recorded at recently deployed USArray stations. They divided the study area into three subregions with lateral scales of ~15° (western, middle, and eastern parts). They reported that the western, middle, and eastern parts show a sharp D″ discontinuity with $\delta V_s = 2.5$ %, no clear evidence for a D″ discontinuity, and a gradual increase in δV_s, respectively. The number of earthquake sources used by the above studies is 10 for Lay and Helmberger (1983), 36 for Young and Lay (1990), 2 for He et al. (2014), and 3 for Sun et al. (2016), respectively, and waveform stacking or waveform forward modeling was used.

It is desirable to infer the detailed S-velocity structure in a broad region beneath the Northern Pacific by analyses using a large number of waveforms for many earthquakes and stations. Since USArray stations have finally moved to the easternmost part of the USA and earthquakes occur in a broad region in the western Pacific, waveform data which are relatively homogeneous in epicentral distance range and sample D″ over a long distance in the E–W direction (Additional file 1: Fig. S1) are now available. This allows us to investigate S-velocity structure beneath the Northern Pacific using a large amount of waveform data for western Pacific earthquakes recorded at North America stations (mainly the USArray).

Our group has developed methods for waveform inversion for three-dimensional (3-D) localized structure and has applied these methods to infer the 3-D S-velocity structure in D″ beneath Central America (Kawai et al. 2014) and the Western Pacific (Konishi et al. 2014). These methods are suitable for analysis of a dataset which consists of a large number of observed waveforms for many earthquakes. Waveform inversion can use not only S and ScS, but also later phases associated with a large velocity contrast in the D″ region (for example, Scd which has its turning point in D″; e.g., Borgeaud et al. 2016). Although these later phases are useful for studying structures in D″, they overlap with other phases at epicentral distances of more than ~80° and thus cannot be used by some other methods.

Data and methods

In this study, we apply the 3-D localized waveform inversion method to a dataset of ~20,000 records including overlapped phases that sample D″ well, and we infer the S-velocity structure in the lowermost 400 km of the mantle beneath the Northern Pacific. We invert the transverse component of broadband waveform data for 131 deep and intermediate earthquakes (orange stars in Fig. 1a, parameters in Additional file 1: Table S1) with $5.5 \leq M_w \leq 7.3$ that occurred in western Pacific subduction zones using receivers in North America from the USArray and other networks (blue inverse triangles in Fig. 1a). The model determined by the inversion gives the 3-D S-velocity wave structure in the D″ region of the target area beneath the Northern Pacific and Alaska (Fig. 1b). The waveform data were downloaded from the Incorporated Research Institutions for Seismology (IRIS) data center. Figure 1a shows event-receiver geometry with great circle ray paths used

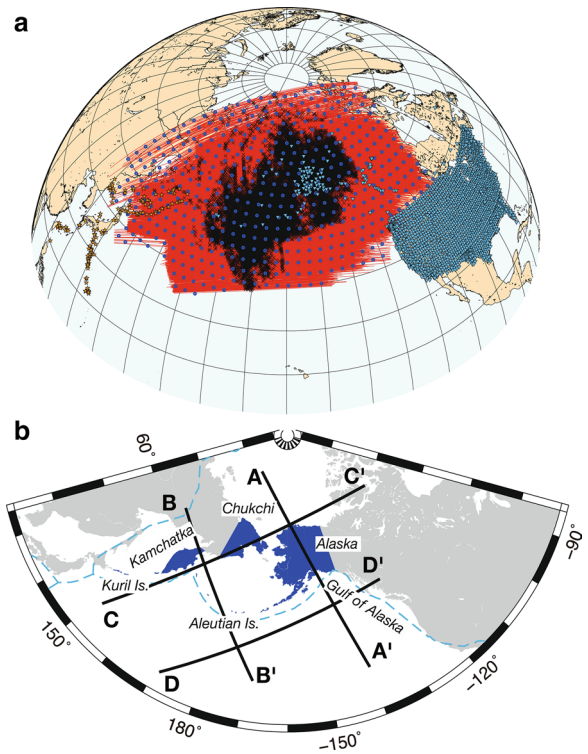

Fig. 1 **a** Event-receiver geometry for the data used in this study. The *great circle* paths which sample the D″ layer are shown in *red*, and crosses indicate the turning points at the CMB. *Light blue reversed triangles* and *orange stars* show the stations in North America, and the 131 intermediate and deep earthquakes (Additional file 1: Table S1), respectively. *Dark blue dots* show the lateral distribution of the perturbation points. **b** The target area of this study. *Black solid lines* show the cross-sections presented in Fig. 3, and *dashed blue curve* shows the current plate boundary (e.g., DeMets et al. 1990)

in this study. We deconvolve the instrument response, apply a band-pass filter to the data, and construct a dataset for the passband from 0.005 to 0.08 Hz (i.e., for the period range 12.5–200 s). We then select records which include data for S, ScS, and other phases that arrive between them.

First, we compute the synthetic seismogram corresponding to each observed record using the Direct Solution Method (DSM; Geller and Ohminato 1994; Kawai et al. 2006) for the anisotropic PREM model (Dziewonski and Anderson 1981) for the Global CMT solutions using boxcar moment rate functions. We apply the same band-pass filter to both the synthetics and the observed records. We select data in the epicentral distance range 70°–100°. We calculate the ratio of the maximum amplitude of each set of observed and synthetic waveforms for each time window and exclude records for which the ratio is greater than 3 or less than 0.33. Then, we use the 'autopick' method (Fuji et al. 2010) to make static corrections for the effect of structure outside the target region. This method picks the S-wave arrival and first peak for all synthetics and measures the time difference between them, Δt, to take the time window from $4\Delta t$ before the S-wave arrival to Δt after the S-wave arrival and compute the cross-correlation for this time window. The peak of the cross-correlation is chosen as the time shift for the static correction for each record. The dataset consists of 19,942 records that satisfy the above criteria; 24,564 records that did not satisfy the criteria were excluded. The histogram for epicentral distance intervals of 5° indicates that the dataset used in this study is relatively homogeneous (Additional file 1: Fig. S1).

Second, we parameterize the 3-D local structure of the target region as a voxelized structure and compute the partial derivatives of the synthetic seismograms with respect to the model parameters for each record and model parameter. In this study, we perturb only the shear modulus, μ, and fix the other parameters (density, ρ, bulk modulus, κ, the quality factor, Q, and the earthquake source parameters). The elastic moduli in the target region are assumed to be isotropic. When we compute the partial derivatives, we use the method of Geller and Hara (1993), which uses the first-order Born perturbation to compute the partial derivatives with respect to the spherically symmetric 1-D starting model (PREM is used in this study). Since the transverse component of waveforms is used in this study, we take into account toroidal-toroidal coupling and neglect other coupling. Synthetic seismograms for voxel perturbations using the first-order Born approximation are represented as follows:

$$\boldsymbol{u}_{3D}(\boldsymbol{r}) = \boldsymbol{u}_{1D}(\boldsymbol{r}) + \sum_{l} \frac{\partial \boldsymbol{u}(\boldsymbol{r})}{\partial m_l} \delta m_l, \tag{1}$$

where $\boldsymbol{u}_{3D}$ is the Born-approximation synthetic seismogram for the 3-D earth model and $\boldsymbol{u}_{1D}$ is the synthetic waveform for the 1-D starting model (PREM in our case).

Finally, we formulate the inverse problem and solve it using the conjugate gradient (CG) method (see Appendix A of Kawai et al. 2014 for details). The linearized inverse problem is usually written as:

$$\boldsymbol{A}\delta\boldsymbol{m} = \delta\boldsymbol{d}, \tag{2}$$

where $\boldsymbol{A}$ is the $N \times M$ matrix of partial derivatives, N is the number of data points, M is the number of model parameters, $\delta\boldsymbol{m}$ is the vector of perturbations to the model parameters with respect to the initial model, and $\delta\boldsymbol{d}$ is the residual vector (the difference of each observed data point and the corresponding point of the synthetic seismogram for the initial model). Since it is well known that the number of unknowns (the number of elements of $\delta\boldsymbol{m}$) is usually smaller than the number of data points (the number of elements of $\delta\boldsymbol{d}$) in geophysical inverse problem (i.e., $M < N$), Eq. (2) is overdetermined and cannot be solved in a rigorous sense. The solution is obtained by solving the normal equations, which are written as follows:

$$\boldsymbol{A}^T\boldsymbol{A}\,\delta\boldsymbol{m} = \boldsymbol{A}^T\delta\boldsymbol{d}. \tag{3}$$

We define a sequence of M mutually orthogonal conjugate vectors (CG vectors) $\boldsymbol{p}_i$ ($i = 1,...,M$),

$$\boldsymbol{p}_j^T\boldsymbol{A}^T\boldsymbol{A}\quad \boldsymbol{p}_i = 0 \quad \text{for } j \neq i, \tag{4}$$

and then we write the solution by summing over the first k vectors

$$\delta\boldsymbol{m}_k = \sum_{j=1}^{k} a_j \boldsymbol{p}_j, \tag{5}$$

where the expansion coefficients a_j are the unknowns. In this study, we choose the value of k which minimizes the Akaike Information Criterion (AIC; see Appendix A of Kawai et al. 2014 for details).

Results

The target region is at latitudes between ~ 35° and 85° and longitudes between ~ 130° and 290° (Fig. 1b) and depths from 0 to 400 km above the CMB. We divide the target region (studied volume) into 150 km × 150 km × 50 km voxels; there are thus 3576 unknown model parameters. We conduct inversion using the first n basis vectors obtained by the CG method. We choose the value of n that minimizes AIC. Additional file 1: Figure S2; Table 1 show the variance and AIC value for each model. When we calculate AIC values, we define the empirical redundancy parameter α (see Appendix A of Kawai

Table 1 Variance and AIC for each model

Model	Variance (%)	AIC
PREM	133.4	–
PREM with time shift	76.2	1620.3
CG6	70.9	1585.6

et al. 2014, for details and definitions). In this study, the AIC value for $\alpha = 2500$ is used. The total number of data points at 1 Hz sampling is 1, 576, 927. The AIC values in Table 1 are thus obtained using the number of independent data, ND $= 1,576,927/(2500 \times 12.5)$. Defining the variance of the data to be 100%, the variance (data minus synthetics) for the PREM synthetics without time shift is 133.4%. A further variance reduction to 76.2% is achieved by making the static corrections. The variance for model CG6, the model obtained for $n = 6$, which minimizes AIC, is 70.9%, as shown in Additional file 1: Fig. S2 and Table 1.

Model CG6 is shown in Fig. 2. To examine the ability of our method to resolve the structure, we conduct synthetic resolution ('checkerboard') tests (Additional file 1: Fig. S3). We confirm that for an ideal noise-free case that the waveform inversion method and dataset used in this study can resolve the lateral heterogeneity well in all the depth ranges for the target region of this study. In order to examine the possible effects of shallow structure, such as the slab beneath North America, on the inversion results, we also checked the independence of the partial derivatives for perturbations in such regions and those in the target region in the lowermost mantle (Additional file 1: Fig. S4). As shown in Additional file 1: Fig. S4, the dataset in this study is large enough to effectively eliminate the trade-off between shallow structure and structure in the target region when all seismograms and all stations are used. Compared to our group's previous studies (e.g., Kawai et al. 2014; Konishi et al. 2014), our present dataset allows us to resolve structure in D″ over a wider horizontal region (about 3000 km in this study, as compared to about 1000 km for Kawai et al. 2014). This facilitates an investigation of how the subducted slabs interact with ambient material in the lowermost mantle beneath the subduction zone.

The S-velocity model obtained by our inversion shows three types of features (Figs. 2, 3):

1. Lateral high-velocity anomalies up to ~3% faster than PREM with a thickness of ~200 km whose lower boundary is ~150 km above the CMB. We can see a prominent sheet-like high-velocity anomaly labeled 'E' in Figs. 2 and 3 extending in the east–west direction to the south of the Aleutian islands at 250–400 km above the CMB, and an arc-like high-velocity anomaly labeled 'F' in Figs. 2 and 3 from the southwest of the Aleutian islands through the east of the Kamchatka peninsula to Chukchi, the eastern tip of Siberia, at 150–250 km above the CMB. We also see two distinct high-velocity regions, labeled F′ and F″ respectively, from 250 to 400 km above the CMB, located directly above 'F'. There is also a sheet-like high-velocity anomaly labeled 'G' in Figs. 2 and 3 beneath southern Alaska at 150–250 km above the CMB.
2. Prominent low-velocity anomalies ~2.5% slower than PREM labeled 'H' in Figs. 2 and 3 are located to the east of the Kamchatka peninsula with a thickness of ~100 km immediately above the CMB beneath the above-mentioned high-velocity anomalies.
3. A relatively thin (~300 km) weak low-velocity anomaly labeled 'I' in Figs. 2 and 3c which is continuous from the low-velocity anomalies beneath the east of Kamchatka peninsula immediately above the CMB to the far east of the Kuril islands to at least 400 km above the CMB.

Discussion

Our model generally agrees with global tomographic models (e.g., French and Romanowicz 2014, 2015), but has finer resolution. Recent waveform forward modeling studies (He et al. 2014; Sun et al. 2016) estimated depths of the D″ discontinuity of ~200 and ~250 km above the CMB beneath Kamchatka and the Northern Pacific, respectively, which are consistent with the depth of the significant high-velocity anomalies between 200 and 300 km above the CMB in our model (Figs. 2, 3). Since the S-velocity anomalies can be primarily attributed to effects of temperature, the high- and low-velocity anomalies indicate colder and hotter than average temperature at each respective depth. Cross-section C–C′ in our model shows that high-velocity anomalies (i.e., relatively cold material) lie at ~250 km above the CMB and that low-velocity anomalies (i.e., relatively hot material) are below the high-velocity anomalies immediately above the CMB. These high-velocity anomalies may be enhanced by the bridgmanite (hereafter referred to as Mg-Pv) to Mg-post-perovskite (hereafter referred to as Mg-PPv) phase transition, because a cold geotherm makes the positive velocity jump associated with the phase transition clearer (Kawai and Tsuchiya 2009).

It has been suggested that some slabs accumulate and stagnate at the mantle transition zone beneath the subduction region. The slab beneath the Aleutian subduction zone, a part of the target region of this study, was found to be stagnant at the bottom of the transition zone (e.g., Gorbatov et al. 2000). If subducted slabs were stagnant in the transition zone, paleosubducted and stagnant

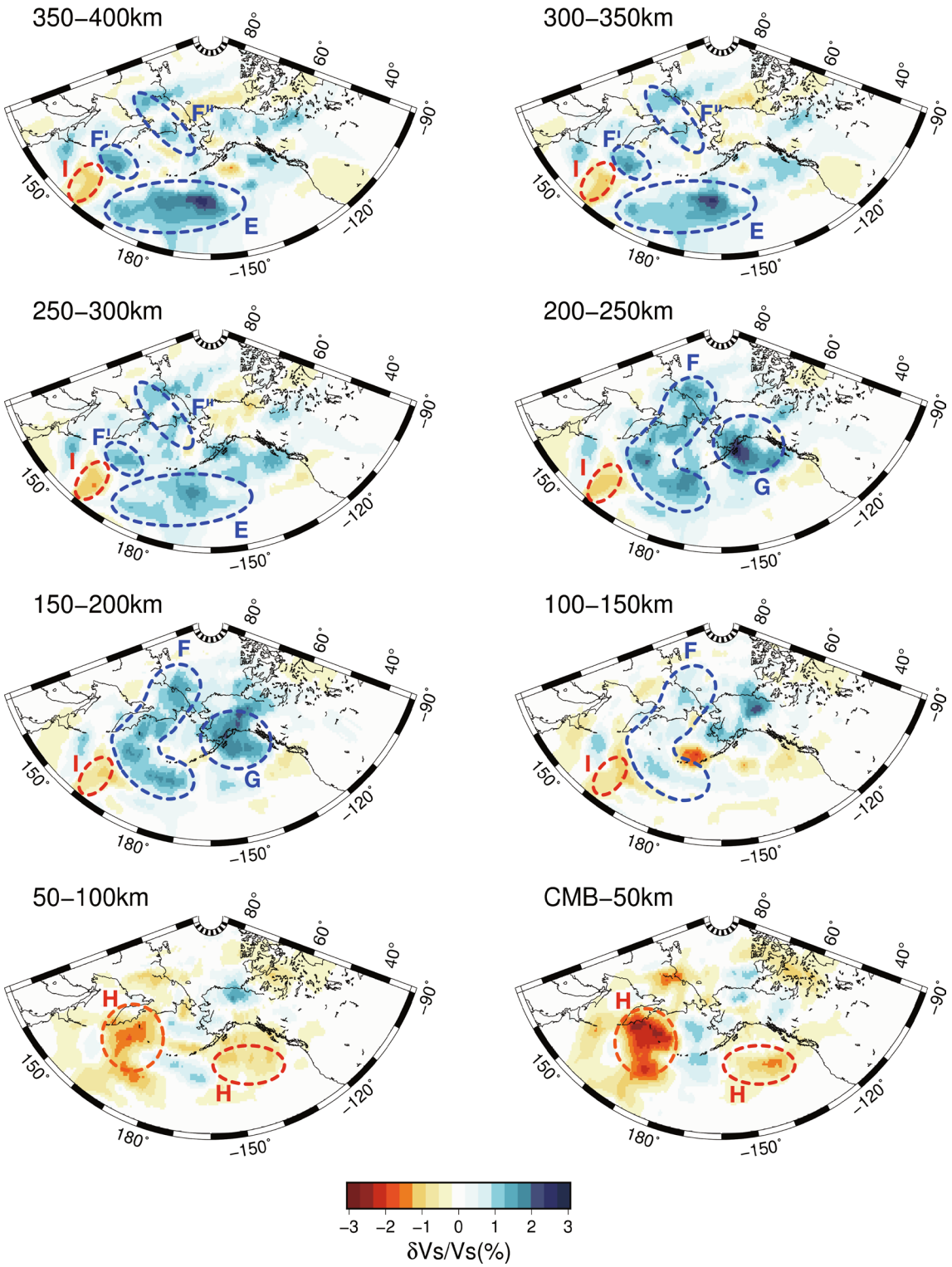

Fig. 2 Results of the inversion (CG6) for the 3-D shear wave velocity structure in the lowermost 400 km of the mantle beneath the Northern Pacific and Alaska for each 50 km depth slice. PREM (Dziewonski and Anderson 1981) is used as the reference model

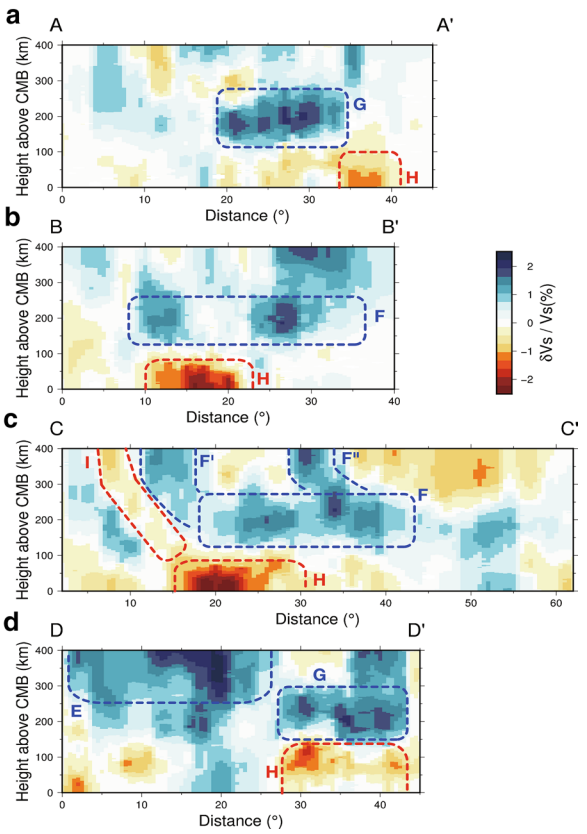

Fig. 3 Cross-section of the inversion for the 3-D shear wave velocity structure (CG6) for cross-sections A–A′, B–B′, C–C′ and D–D′, which are shown in Fig. 1b

slabs would have begun to avalanche and descend into the lower mantle in about 10 million years (Pysklywec and Ishii 2005) and would have finally reached the CMB. Whether they stagnate or penetrate the 660 km discontinuity, subducted slab materials would descend to the lower mantle and reach the CMB. Hence, the high-velocity anomalies shown in our model could be interpreted as the paleosubducted cold slab. If the subduction rate is about 2 cm/year in the lower mantle, it would take about 100 million years for slabs to descend from the surface to the CMB in this region. Taking this into account, the sharp high-velocity anomalies in D″ found in our model could be remnants of the paleosubducted Kula or Pacific plate slab (e.g., Lithgow-Bertelloni and Richards 1998). The velocity contrast may be enhanced by the Mg-Pv to Mg-PPv phase transition, due to the low temperature. Two high-velocity anomalies (labeled F′ and F″, respectively) continuous from the slab remnants to 400 km above the CMB are found in cross-section C−C′ in our model. These two high-velocity anomalies shown in cross-section C–C′ (Fig. 4) imply the possibility of two different subducting slabs (e.g., Kula and Pacific).

Strong low-velocity anomalies with a thickness of ~ 100 km exist immediately above the CMB below the cold slab remnants (Figs. 3c, 4). These strong low-velocity anomalies can be attributed to the TBL caused by the blanketing effect of the horizontally lying cold slab. Our model also shows a low-velocity anomaly continuous from the CMB to at least 400 km above the CMB (Figs. 2, 3c); this could be an upwelling plume that is deflected around the descending cold slab material (Fig. 4). Previous numerical mantle convection studies are supportive of the hypothesis that the subducted slab causes plume-like upwelling (Tan et al. 2002; Tackley 2011; Bower et al. 2013). On the other hand, this study suggests that the hot materials in the TBL developed beneath the cold slab remnants might produce upwelling (a passive plume) along the subducted slab.

Our results are generally consistent with previous studies in terms of the location of the low-velocity anomaly. For example, the models of He et al. (2014) and French and Romanowicz (2014, 2015) show a low-velocity anomaly beneath Kamchatka continuous from the CMB to 850 km, and to about 500 km above the CMB, respectively.

Conclusions

We conducted localized waveform inversion for the three-dimensional S-velocity structure in D″ beneath the Northern Pacific. Our obtained S-velocity model showed three features. (1) There are prominent sheet-like lateral high-velocity anomalies up to ~3% faster than PREM with a thickness of ~200 km whose lower boundary is ~150 km above the CMB. There are also high-velocity anomalies extending in the east–west direction in the south of the Aleutian islands at 300–400 km above the CMB and south of Alaska at 150–250 km above the CMB, respectively. There is an arc-like high-velocity anomaly from southwest of the Aleutian islands through

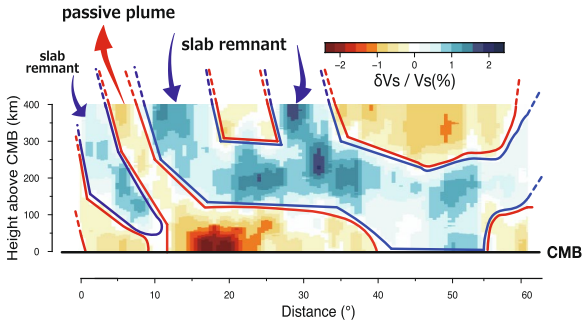

Fig. 4 Schematic interpretation based on profile C–C′ in Figure 3. The basal thermal boundary layer is thicker beneath the subducted slab materials and a 'passive plume' has developed along the subducted slab remnants

the east of the Kamchatka peninsula to Chukchi, the eastern tip of Siberia, at 150–200 km above the CMB. (2) A prominent low-velocity anomaly, which is ~2.5% slower than PREM, is located to the west of the Kamchatka peninsula, immediately above the CMB beneath the high-velocity anomalies. (3) There is a relatively thin (~300 km) low-velocity structure continuous from the low-velocity anomaly "(2)" to at least 400 km above the CMB. We also detected a continuous low-velocity anomaly from the east of Kamchatka peninsula at 50 km above the CMB to the far east of the Kuril islands at 400 km above the CMB.

Assuming the velocity anomalies are due primarily to the effects of temperature, we interpret the above features as follows. (1) There are remnants of subducted slab materials which are stagnant ~150 km above the CMB. Furthermore, the Mg-Pv to Mg-PPv phase transition could enhance high-velocity anomalies in the slab due to the cold geotherm; (2) hot and less dense material develops beneath the subducted cold slab remnants; (3) the hot and less dense material ascends along subducted cold slab remnants and forms a passive plume (Fig. 4).

Additional file

Additional file 1. Details and validity checks.

Authors' contributions

YS, KKa and RJG wrote the manuscript, YS, KKa, KKo and RJG improved and extended the algorithms used in the inversion, YS, AFEB and KKo performed data analysis, KKa and RJG designed the project, AFEB and KKo helped with the design and evaluation of the project. All authors read and approved the final manuscript.

Author details

[1] Department of Earth and Planetary Science, School of Science, University of Tokyo, Hongo 7-3-1, Bunkyo-ku, Tokyo 113-0033, Japan. [2] Institute of Earth Sciences, Academia Sinica, 128 Academia Road Sec. 2, Nangang, Taipei 11529, Taiwan.

Acknowledgements

We thank Barbara Romanowicz and Satoru Tanaka for their thoughtful comments and suggestions. This research was partly supported by grants from the Japanese Ministry of Education, Science and Culture (Nos. 16K05531, 15K17744 and 15H05832). Some figures were made with GMT (http://gmt.soest.hawaii.edu). We thank the Incorporated Research Institutions for Seismology (IRIS) for making a large dataset of high-quality data available freely. We used the waveform data from following networks: 6E (Wabash Valley Seismic Zone), 7A (MAGIC), AK (Alaska Regional Network), AZ (ANZA Regional Network), BK (Berkeley Digital Seismic Network, BDSN), CI (Southern California Seismic Network, SCSN), CN (Canadian National Seismic Network, CNSN), IU (Global Seismograph Network, GSN-IRIS/USGS), LB (Leo Brady Network), LD (Lamont-Doherty Cooperative Seismographic Network, LCSN), NN (Nevada Seismic Network), TA (USArray Transportable Array), UO (University of Oregon Regional Network), US (United States National Seismic Network, USNSN), UU (Utah Network), XD (Mount St Helens aka iMUSH), XN (Canadian Northwest Experiment, CANOE), XO (OIINK (AKA SDYNAC)), XR (SIEDCAR/UTA), XT (W Idaho Shear Zone BB/UF), XU (CAFE/UW), XV (Big Horn/UC Boulder), YW (Resolving structural control of episodic tremor and slip along the length of Cascadia, FACES/Berkeley), YX (NE-NV BB/Stanford), Z9 (Southeastern Suture of the Appalachian Margin Experiment, SESAME).

Competing interests

The authors declare that they have no competing interests.

Received: 3 August 2016 Accepted: 23 November 2016
Published online: 01 December 2016

References

Borgeaud AFE, Konishi K, Kawai K, Geller RJ (2016) Finite frequency effects on apparent S-wave splitting in the D″ layer: comparison between ray theory and full-wave synthetics. Geophys J Int 207:12–28

Bower DJ, Gurnis M, Sun D (2013) Dynamic origins of seismic wave speed variation in D″. Phys Earth Planet Inter 214:74–86

DeMets C, Gordon RG, Argus DF, Stein S (1990) Current plate motions. Geophys J Int 101:425–478

Dziewonski AM, Anderson DL (1981) Preliminary reference earth model. Phys Earth Planet Inter 25:297–356

French SW, Romanowicz BA (2014) Whole-mantle radially anisotropic S-velocity structure from spectral-element waveform tomography. Geophys J Int 199:1303–1327

French SW, Romanowicz BA (2015) Broad plumes rooted at the base of the Earth's mantle beneath major hotspots. Nature 525:95–99

Fuji N, Kawai K, Geller RJ (2010) A methodology for inversion of broadband seismic waveforms for elastic and anelastic structure and its application to the mantle transition zone beneath the northwestern pacific. Phys Earth Planet Inter 180:118–137

Garnero EJ, McNamara AK (2008) Structure and dynamics of Earth's lower mantle. Science 320:626–628

Geller RJ, Hara T (1993) Two efficient algorithms for iterative linearized inversion of seismic waveform data. Geophys J Int 115:699–710

Geller RJ, Ohminato T (1994) Computation of synthetic seismograms and their partial derivatives for heterogeneous media with arbitrary natural boundary conditions using the direct solution method. Geophys J Int 116:421–446

Gorbatov A, Widiyantoro S, Fukao Y, Gordeev E (2000) Signature of remnant slabs in the North Pacific from P-wave tomography. Geophys J Int 142:27–36

He Y, Wen L, Zheng T (2014) Seismic evidence for an 850 km thick low-velocity structure in the Earth's lowermost mantle beneath Kamchatka. Geophys Res Lett 41:7073–7079

Hutko A, Lay T, Garnero E, Revenaugh J (2006) Seismic detection of folded subducted lithosphere at the core–mantle boundary. Nature 441:333–336

Kawai K, Tsuchiya T (2009) Temperature profile in the lowermost mantle from seismological and mineral physics joint modeling. Proc Nat Acad Sci 106:22119–22123

Kawai K, Takeuchi N, Geller RJ (2006) Complete synthetic seismograms up to 2 Hz for transversely isotropic spherically symmetric media. Geophys J Int 164:411–424

Kawai K, Konishi K, Geller RJ, Fuji N (2014) Methods for inversion of body-wave waveforms for localized three-dimensional seismic structure and an application to D″ structure beneath central America. Geophys J Int 197:495–524

Konishi K, Kawai K, Geller RJ, Fuji N (2014) Waveform inversion for localized three-dimensional seismic velocity structure in the lowermost mantle beneath the western Pacific. Geophys J Int 199:1245–1267

Lay T, Helmberger DV (1983) The shear-wave velocity gradient at the base of the mantle. J Geophys Res 88:8160–8170

Lithgow-Bertelloni C, Richards MA (1998) The dynamics of Cenozoic and Mesozoic plate motions. Rev Geophys 36:27–78

Pysklywec RN, Ishii M (2005) Time dependent subduction dynamics driven by the instability of stagnant slabs in the transition zone. Phys Earth Planet Inter 149:115–132

Sun D, Helmberger D, Miller MS, Jackson JM (2016) Major disruption of D″ beneath Alaska. J Geophys Res 121:3534–3556

Tackley PJ (2011) Living dead slabs in 3-D: the dynamics of compositionally-stratified slabs entering a "slab graveyard" above the core-mantle boundary. Phys Earth Planet Inter 188:150–162

Tan E, Gurnis M, Han L (2002) Slabs in the lower mantle and their modulation of plume formation. Geochem Geophys Geosyst 3(11):1067. doi:10.1029/2001GC000238

van der Hilst RD, de hoop MV, Wang P, Shim SH, Ma P, Tenorio L (2007) Seismostratigraphy and thermal structure of Earth's core–mantle boundary region. Science 315:1813–1817

Wysession ME, Lay T, Revenaugh J, Williams Q, Garnero EJ, Jeanloz R, Kellogg LH (1998) The D″ discontinuity and its implications. In: Gurnis M, Wysession M, Knittle E, Buffett BA (eds) The Core–Mantle boundary region, vol 28 of AGU Geodynamics Series, American Geophysical Union, pp 273–297

Young CJ, Lay T (1990) Multiple phase analysis of the S-velocity structure in the D″ region beneath Alaska. J Geophys Res 95:17385–17402